Flange Local Buckling of Pultruded GFRP Box Beams

Tianqiao Liu[1] and Kent A. Harries[2,3]

Abstract

An experimental program investigating the flange local buckling (FLB) behavior of pGFRP box-sections is reported. The commonly accepted design equation based on plate theory was validated although importance of accurate assessment of the rotational stiffness of the web-flange junctions was identified. It is concluded that the lower bound solution, assuming the flange is a simply-supported plate subject to uniform compressive stress, results in uniformly conservative predictions of the critical FLB moments. The theoretical solution accounting for flange plate edge support stiffness based only on web stiffness, material and geometric properties of the cross section over predicts the support stiffness resulting in unconservative predictions of FLB behavior. The rotational stiffness of flange-web junction of the pGFRP box-section is also investigated experimentally. It is found that the actual rotational stiffness of flange-web junction is relatively low, closer to the simply-supported boundary condition. The role of fiber architecture at the web-flange junction is identified as affecting this behavior. The conclusions of this study support the use of the lower bound solution for design of pGFRP box-sections.

Keywords: pultruded GFRP, flexural stability, flange local buckling

Notation

b	total width of section
b_f	centerline flange width; $b_f = b - t_w$
b_w	centerline web depth; $b_w = d - t_f$
D_{ij}	plate flexural stiffness parameters: $D_{11} = E_L t^3/12(1 - v_{LT}v_{TL})$; $D_{22} = E_T t^3/12(1 - v_{LT}v_{TL})$; $D_{12} = v_{LT}D_{22}$; $D_{66} = G_{LT}t^3/12$; superscripts indicate flange (f) or web (w).
d	total depth of section
E_L	modulus of elasticity in longitudinal direction determined from tension (E_{Lt}), compression (E_{Lc}) or flexure tests (E_{Lf})
E_T	modulus of elasticity in transverse direction
F_{Lc}	compressive strength in longitudinal direction

[1] Postdoctoral Associate, Department of Civil and Environmental Engineering, University of Pittsburgh, Pittsburgh, USA.
[2] Bicentennial Board of Visitors Faculty Fellow and Associate Professor, Department of Civil and Environmental Engineering, University of Pittsburgh, Pittsburgh, USA. kharries@pitt.edu
[3] Leverhulme Visiting Professor, BRE Centre for Innovative Construction Materials, University of Bath, UK.

f_{cr} critical buckling stress

G_{LT} in plane shear modulus

h width of test specimen in web-flange junction test

k spring constant, simulating elastic rotational stiffness at flange edge support

K effective column length factor

L length of column or clear length of flange in web-flange junction test

L_b laterally unbraced length of beam

M_{cr} critical buckling flexural strength

P_{cr} critical buckling load

r radius of gyration; subscripts indicate strong (x) or weak (y) axis.

t flange or web thickness, for pGFRP it is typical that $t_f = t_w$

ν_{LT} major Poisson's ratio of orthotropic plate

ν_{TL} minor Poisson's ratio of orthotropic plate; $\nu_{TL} = \nu_{LT} E_T/E_L$

Δ vertical displacement

Introduction

Pultruded glass fiber reinforced polymer (pGFRP) structural profiles are seeing wider adoption in the field of civil infrastructure applications, including pedestrian bridges, cooling towers and low-rise modular structures. As a result, pGFRP section are being applied in a wide variety of axial and flexural load-carrying applications. In the direction of pultrusion (longitudinal axis of member), pGFRP composite materials have tensile and compressive strength comparable to that of mild steel, although the modulus of elasticity is only about one-tenth that of steel. In the transverse direction, strength and modulus vary, but are typically three to five times lower than in the longitudinal direction. The low modulus and high anisotropy, as well as the commonly used thin-walled profiles, result in pGFRP structural members that tend to exhibit large deflections and buckling instabilities before the material strength limit state is achieved. pGFRP flexural members, such as pGFRP I- and box-sections, may experience flange and/or web local buckling (FLB and WLB), global lateral torsional buckling (LTB) or, at intermediate lengths, an instability characterized by the interaction between local and global buckling. The present work concentrates on FLB dominated buckling behavior; in order to mitigate interaction with LTB, the case of flexure about the weak axis of a rectangular box-section is considered.

In the past decades, flange local buckling behavior of pGFRP sections has been investigated by many researchers. Nonetheless, only eight tests reporting FLB of box sections (all 100 x 100 x 4.3 mm) are known (Barbero et al. 1991). Since few flexural tests on pGFRP box-sections are known in the literature, it is

informative to consider studies of the axial load behavior of pGFRP box-sections exhibiting local buckling and flexural tests of I-sections in order to understand some of the factors affecting FLB behavior of pGFRP. Short axial load carrying pGFRP box-sections (stub columns) exhibit either crushing (not relevant to present study) or local buckling (e.g., Zureick and Scott 1997; Seangatith and Sriboonlue 1999; and Hashem and Yuan 2001). As would be expected for column members, the cross sections studied previously typically have compact flange plates and none of the cited works establish a relationship between wall slenderness and failure mode. Cardoso et al. (2014a) reported 74 concentric axial load tests of square pGFRP box-sections. Of these, 15 short columns (all having $KL/r < 30$) having flange width-to-thickness ratios, b/t, equal to 13.9 or 15.8 exhibited FLB-dominated behavior. Cardoso et al. also present a method and examples of the calculation of axial capacity of pGFRP box sections accounting for both local plate (i.e., wall) and global member slenderness and addressing both local and global imperfections. Cardoso et al. (2014b) presents related closed form equations for local buckling of pGFRP box shape and other sections.

Analysis of previous experimental investigations of FLB behavior of I-sections subject to flexure identify flange slenderness (e.g., Pecce and Cosenza 2000 and Correia et al. 2011) and the relatively poor rotational restraint provided by the web (Bank et al. 1996) as affecting FLB behavior. Both effects suggest that box-sections may be a more efficient shape for pGFRP flexural members. A limitation of most available previous studies on I-sections is that only two flange slenderness ratios, $b/2t \approx 8$ and 12 have been reported. More recently, Vieira et al. (2017) reported 62 four-point flexure tests on pGFRP I-sections having flange slenderness ratios ranging from $b/2t \approx 6$ to 12. In order for FLB to be observed, $b/2t > 8$ and the unbraced length, $L_b/r_y < 50$. Vieira et al. also demonstrated that extant code/standard-based equations for calculating FLB capacity significantly underestimate that seen in experiments on I-sections.

To predict the critical flange local buckling load of pGFRP box-sections, plate theory and the energy method are typically used. Barbero et al. (1991) adopted the classic expression of composite plate bending (Eq. 1) and used an approximate shape function (Eq. 2) to calculate critical FLB stress.

$$D_{11}\frac{\partial^4 w}{\partial x^2} + 2(D_{12} + 2D_{66})\frac{\partial^4 w}{\partial x^2 \partial y^2} + D_{22}\frac{\partial^4 w}{\partial y^4} + f_x\frac{\partial^2 w}{\partial x^2} = 0 \tag{1}$$

Where D_{ij} are the flexural stiffness parameters for a homogenous orthotropic plate (given in list of notations) and w is the out of plane shape given by Eq. 2 in which x is the longitudinal direction of the member and y is the transverse dimension of the compression flange.

$$w(x, y) = \sum_{m-1}^{\infty} f_m(y)\sin\frac{m\pi x}{a} \tag{2}$$

Prior to Barbero et al., the flange plates of pGFRP sections were commonly assumed to be either simply-supported or fully restrained at the flange edges, which under- or over-estimated the true critical FLB stress, respectively. To overcome this limitation, Barbero et al. proposed to use the transverse plate bending

stiffness of the web, D_{22}^{w}, to simulate the elastic rotational restraint of the compression flange at its edges . This significantly improved the accuracy of critical FLB stress predictions. Using Barbero's approach, however, a system of transcendental equations must be solved, making the approach cumbersome.

Pecce and Cosenza (2000) proposed an empirical relationship for predicting the critical FLB stress of pGFRP I-sections, as:

$$f_{cr} = c_1 c_2 \left[\frac{\pi^2 D_{11}^{f}}{(b/2)^2 t_f} \right] \tag{3}$$

Where c_1 and c_2 are empirical coefficients accounting for rotational restraint at the flange edge support and orthotropy of the material, respectively. The term in brackets is the classic equation for the critical buckling stress of a simply-supported isotropic plate subject to uniaxial compression. Although Pecce and Cosenza successfully achieved a simple closed-formed equation, their approach is highly empirical and, due to the lack of available data on box-sections, is derived considering only pGFRP I-sections. Ascione et al. (2016) and Cardoso and Vieira (2017) also report closed form solutions for local buckling of pGFRP I-sections.

Qiao et al. (2001) employed the same method used by Barbero et al. (1991), although with a simpler shape function, to derive the equation for predicting the critical FLB stress of pGFRP box-sections. Qiao et al. proposed a modified expression for the elastic rotational restraint at the flange edge support: modifying D_{22}^{w} by a factor that depends on the material and geometry of the web plates. Once again, this approach requires the solution of a transcendental equation.

Based on plate theory, Kollár (2003), establishing a benchmark for the field, proposed a suite of explicit equations for predicting the critical FLB stress for pGFRP sections. In Kollár's work, a more refined prediction of the elastic rotational restraint at the flange edge support of pGFRP box-sections was proposed, as:

$$k = \frac{4 D_{22}^{w}}{b_w} \left[1 - \frac{\left(t_f f_{cr,ss}^{f} \right) a_{11}^{f}}{\left(t_w f_{cr,ss}^{w} \right) a_{11}^{w}} \right] \tag{4}$$

Where a_{11}^{f} and a_{11}^{w} account for the thickness and material properties of the flange and web. For most available pultruded shapes, especially box-sections, $a_{11}^{f} = a_{11}^{w}$. $f_{cr,ss}^{f}$ and $f_{cr,ss}^{w}$ are the critical buckling stresses of the simply-supported orthotropic flange and web plates subject to uniform compression, respectively, given as (Lekhnitskii 1968):

$$f_{cr,ss}^{f} = \frac{\pi^2}{b_f^2 t_f} \left[2\sqrt{D_{11}^{f} D_{22}^{f}} + 2\left(D_{12}^{f} + 2 D_{66}^{f} \right) \right] \tag{5}$$

$$f_{cr,ss}^{w} = \frac{\pi^2}{b_w^2 t_w}\left[13.9\sqrt{D_{11}^{w} D_{22}^{w}} + 11.1\left(D_{12}^{w} + 2D_{66}^{w}\right)\right] \tag{6}$$

In Kollár's expression of the so-called *k*-factor (Eq. 4), not only the classic form, $k = D_{22}^{w}/b_w$, is adopted, but also the flexural behaviors of both flange and web plates are considered.

Existing consensus design guides address FLB of box-sections in variations of the same manner. Each adopts the analytic solution for an infinitely long plate, supported along its transverse edges subject to a uniform compression field.

$$f_{cr} = \frac{\pi^2}{t_f b_f^2}\left[\alpha\sqrt{D_{11}^{f} D_{22}^{f}} + \beta\left(D_{12}^{f} + 2D_{66}^{f}\right)\right] \tag{7}$$

Each standard prescribes different values for α and β. EUR 27666 (2016) provides lower and upper bounds of FLB critical stress values without additional guidance. The lower bound critical buckling stress corresponds to the simply-supported plate for which $\alpha = \beta = 2$, while the upper limit corresponds to the case of a plate fixed against rotation along both transverse edges: $\alpha = 4.53$ and $\beta = 2.44$. The 2010 ASCE *Prestandard* (ASCE 2010) adopted Kollar's (2003) equations to better define the critical stress between these limits by defining α and β to account for the rotational stiffness of the flange support. By rearranging Kollar's equation, the following formulations for α and β are found:

$$\alpha = 2\sqrt{1 + \frac{4.139 k b_f}{k b_f + 10 D_{22}^{f}}} \tag{8}$$

$$\beta = 2 + 0.62\left(\frac{k b_f}{k b_f + 10 D_{22}^{f}}\right)^2 \tag{9}$$

This approach was deemed unnecessarily complex for design equations and is unlikely to find its way into the anticipated ASCE *Standard*. In any case, the equations promulgated in design guides are based on plate theory solutions and – due to the lack of available data – have not been validated with experimental results.

Experimental Program

In this work, an experimental program of four-point flexure tests, was conducted on pGFRP box-sections to investigate flange local buckling (FLB) behaviour. In order to have a relatively high flange slenderness and mitigate the lateral torsional buckling behaviour, two 102 x 152 x 6.4 mm rectangular box-sections (denoted B1 and B2) were tested in weak-axis flexure. Indeed, preliminary tests on square pGFRP box-sections, as well as fundamental calculations of capacity, indicated that FLB is not likely a dominate limit state in square box sections or those bent about their strong axis. In each beam it was found that the two 152 mm flange plates had considerably different thickness (presumably resulting from a misalignment of

the inner and outer pultrusion dies). Thus, each test specimen was further denoted F1 or F2 to indicate their orientation during testing – whether flange 1 or 2 is the compression flange. The measured cross section geometries of the specimens are shown in Table 1. Since significant damage to pGFRP beams may occur when tested in the post-buckling range or when loaded close to the material strength limit state, in this work, all tests were conducted in the linear range of the material, permitting each specimen (B1 and B2) to be tested in both orientations (F1 or F2 in compression). Additionally, the specimens were tested over decreasing span lengths. This approach to testing the same specimens multiple times – ensuring only limited elastic buckling – has been demonstrated in previous studies including Vieira et al. (2017).

Table 1 Specimen geometries

Beam Specimen	B1		B2	
nominal designation, *d x b x t*	102 x 152 x 6.4 mm			
Compression flange	F1	F2	F1	F2
depth, d	101.5 mm		101.4 mm	
flange width, b	152.3 mm		152.3 mm	
flange thickness, t_f	7.08 mm	6.07 mm	6.98 mm	6.07 mm
b/t_f	21.5	25.1	21.8	25.1
web thickness, t_{w1}	6.25 mm		6.29 mm	
web thickness, t_{w2}	6.74 mm		6.70 mm	

The pGFRP box sections used were fabricated with a fire retardant polyester (PE) resin. The 6.4 mm wall thickness contains three rovings of primary reinforcement and has a fibre volume ratio, V_f = 0.37. The experimentally determined material properties of the pGFRP box-sections are given in Table 2. Tested samples were obtained from both F1 and F2 of both B1 and B2; the average results are shown with the variation across all specimens (COV = 0.09). It can be seen that measured properties are all greater than the manufacturer-reported values as well as the minimum requirements prescribed by ASCE (2010). In all subsequent calculations in this work, the measured material properties are used.

Table 2 Mechanical properties of pGFRP box-sections

Mechanical property	Test method	Experimentally obtained value (COV)	Manufacturer reported value	ASCE (2010) minimum requirement
		Flange	Flange/Web	Flange/Web
E_{Lt} (MPa)	ASTM D3039	21824 (0.09)	17200	20685
E_{Lc} (MPa)	ASTM D695	21367 (n.a.)	17200	20685
E_T (MPa)	nonstandard[1]	11260 (0.03)	5500	5516
E_{Lf} (MPa)	ASTM D7264	18485 (0.08)	12400	n.a.
G_{LT} (MPa)	ASTM D3518	3399 (0.03)	3100	2758
F_{Lc} (MPa)	ASTM D695	270 (n.a.)	207	207
ν_{LT}	ASTM D3039	0.29 (n.a.)	n.a.	0.30[2]

[1] see Liu et al. (2017)
[2] in absence of test data, 0.30 is permitted by ASCE (2010).

Following the test method described by Vieira et al. (2017), all specimens were tested in the 900-kN capacity four-point bending test set-up shown in Figure 1a. Specimens, B1 and B2, were tested over the span configurations, shown in Table 3. Three electrical resistance strain gages spaced at $b/2$ = 75 mm, centred on the midspan, were installed on the compression flanges of each specimen (Figure 1b). The expected buckling half-wave length for a box-section is b; therefore, this gage arrangement is sufficient to capture buckling behaviour.

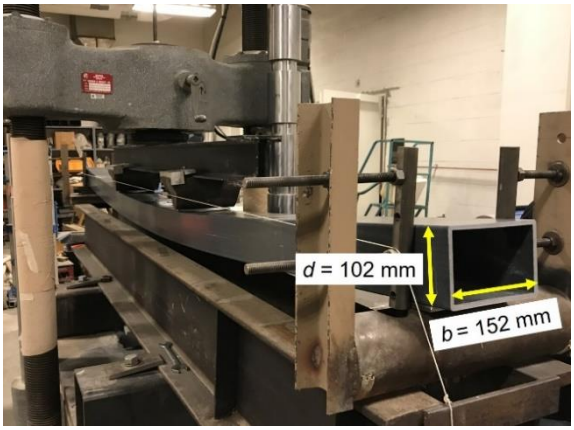

a) Four-point bending test set-up (B2-F2-900 shown)

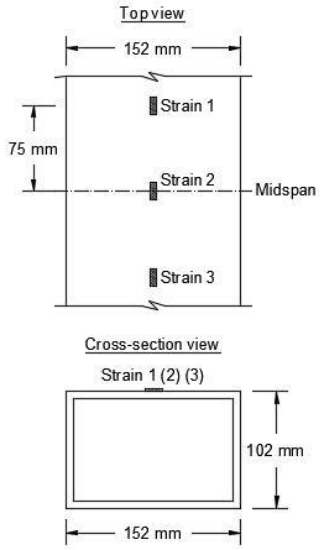

b) Strain gage layout in constant moment region for each test arrangement

Figure 1 Four-point bending test set up and instrumentation

Table 3 Test configurations

Test[1]	Shear span (mm)	Constant moment region (cmr) (mm)	Simple span (mm)	Test set-up
B1-F1-700	750	700	2200	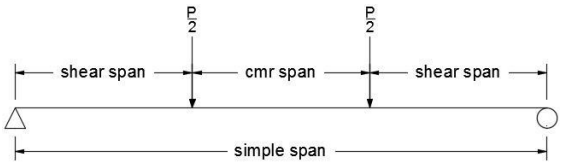
B1-F1-800	800	800	2400	
B1-F2-700	750	700	2200	
B1-F2-800	800	800	2400	
B2-F1-900	900	900	2700	
B2-F1-1000	850	1000	2700	
B2-F1-1100	800	1100	2700	
B2-F2-900	900	900	2700	
B2-F2-1000	850	1000	2700	
B2-F2-1100	800	1100	2700	

[1]test designation: [beam]-[compression flange]-[cmr span]; that is, B1-F1-700 corresponds to beam B1 tested such that flange F1 is in compression over constant moment region of 700 mm.

Determination of FLB Moment

The moment-strain curves obtained during testing were used to determine the critical FLB moments. An example is shown in Figure 2a in which the critical buckling moment, M_{cr} = 8267 Nm is determined from the obvious bifurcation of, in this case, strain gage 2 (see Figure 1b). An image of the compression flange of the same specimen is shown in Figures 2b and c. The flange buckling is readily apparent. Strain gage 2, located at midspan, is clearly located on the tension side of the buckle as indicated by the strains shown in Figure 2a. Additionally, the buckle half-wave length, equal to 156 mm, is determined as half the distance between peak amplitudes, in this case 313 mm (Figure 2c), very close to the expected value of 152 mm, the box-section flange width. The critical buckling moments for all tests are given in Table 4 and all moment-strain curves are provided in Appendix A.

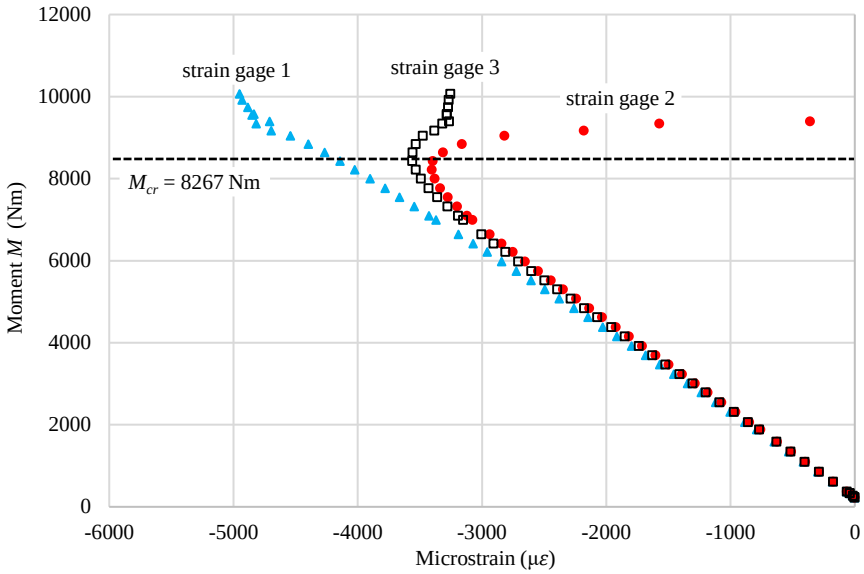

a) Moment-strain response; M_{cr} = 8267 Nm

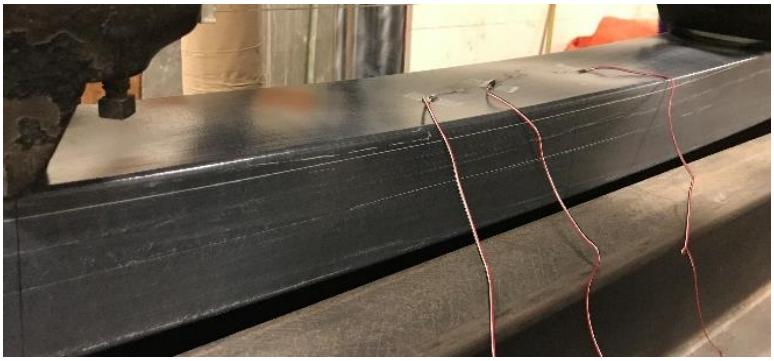

b) Compression flange buckling of constant moment region showing 5 half buckling waves

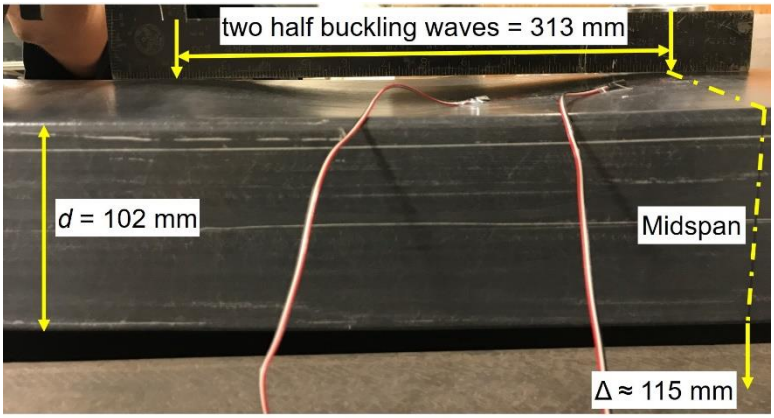

c) Image of compression flange buckling near midspan

Figure 2 Compression flange behavior of specimen B2-F2-900

Comparisons with Predicted FLB Buckling Capacity

In Table 4, experimentally determined critical FLB moments were compared with lower ($\alpha = \beta = 2$) and upper ($\alpha = 4.53$ and $\beta = 2.44$) bound predictions given by Eq. 7. The lower bound predictions are often used in design. The values between lower and upper bound predictions reflect the rotational stiffness of the flange supports at the web; where the lower bound represents a simply-supported condition along the edges of the compression flange and the upper bound a fixed condition. Kollár (2003) provides a method of calculating the elastic rotational stiffness of edges supporting the box-section compression flange and therefore is thought to represent a more accurate solution. For the box section tested, Kollár's formulation (Eqs. 8 and 9) leads to parameters $\alpha = 3.00$ and $\beta = 2.06$ for flange F1 and $\alpha = 3.30$ and $\beta = 2.11$ for flange F2.

In the analytical predictions shown in Table 4 measured geometric and material properties (Tables 1 and 2) are used. For simplicity, the average web thickness, $t_w = 6.50$, was used when required. In all calculations, the longitudinal modulus determined for flexural tests, E_{Lf}, is used to characterise flange buckling behaviour as recommended by Cardoso (2014) in relation to FLB of axially loaded members and Liu (2017) in relation to FLB of members in flexure. The necessity of using E_{Lf} in flange buckling formulations is described at length in Liu et al. (2018).

As expected, the experimentally obtained results fall between the ideal lower and upper bound predictions and tend to fall closer to the lower bound. Additionally, the calculation (Eq. 4) that includes the effect of rotational stiffness of the flange edge support (Kollár 2003) overestimates the experimentally observed values. None of these ideal calculations account for imperfections or variations in geometry or material properties; and thus, the over-prediction should not be unexpected. This observation is reinforced by the fact that the overestimation is somewhat proportional to the length over which buckling occurs (the constant moment region). The longer spans have more buckling half waves and, as a result, generally exhibit a lower capacity. Furthermore, the calculation of the flange edge support rotation stiffness, itself, is ideal and may therefore tend to overestimate this stiffness. Like plate flexural properties (Liu et al. 2018), the rotational stiffness of the flange edge support will be impacted by the fibre architecture as the fibre rovings transition from flange to web.

The calculations in Table 4 use measured material properties. For design, nominal or manufacturer-reported properties are likely to be used. In this case, using manufacturer-reported properties rather than measured properties (see Table 2) in Eq. 7 results in reduction in all predicted values of approximately 40%. While safely conservative, such under prediction of capacity results in inefficient material utilisation.

Table 4 Experimentally and analytically determined critical FLB moments

Tests	-	Experimentally determined critical FLB moments	Analytically determined critical FLB moments							
			lower bound solution		k calculated by Eq. 4		upper bound solution		k_{eff}	
	F1	-	$\alpha = \beta = 2$		$\alpha = 3.00$; $\beta = 2.06$		$\alpha = 4.53$; $\beta = 2.44$		$\alpha = 2.36$; $\beta = 2.01$	
	F2	-			$\alpha = 3.30$; $\beta = 2.11$				$\alpha = 2.44$; $\beta = 2.01$	
	b/t_f	M_{cr} (Nm)	M_{cr}	pred/exp	M_{cr}	pred/exp	M_{cr}	pred/exp	M_{cr}	pred/exp
B1-F1-700	21.5	12558	10634	0.85	13933	1.11	19615	1.56	11764	0.94
B1-F1-800	21.5	12310	10634	0.86	13933	1.13	19615	1.59	11764	0.96
B1-F2-700	25.1	9954	7238	0.73	10200	1.02	13351	1.34	8193	0.82
B1-F2-800	25.1	9207	7238	0.79	10200	1.11	13351	1.45	8193	0.89
B2-F1-900	21.8	10315	10226	0.99	13490	1.31	18861	1.83	11355	1.10
B2-F1-1000	21.8	11414	10226	0.90	13490	1.18	18861	1.65	11355	0.99
B2-F1-1100	21.8	12059	10226	0.85	13490	1.12	18861	1.56	11355	0.94
B2-F2-900	25.1	8267	7218	0.87	10170	1.23	13313	1.61	8171	0.99
B2-F2-1000	25.1	7216	7218	1.00	10170	1.41	13313	1.85	8171	1.13
B2-F2-1100	25.1	7425	7218	0.97	10170	1.37	13313	1.79	8171	1.10

Elastic Rotational Stiffness of Flange Edge Support

Elastic rotational stiffness of flange edge support consists of the stiffness of flange-web junction and the rotational stiffness imparted by the web. Conventionally, the contribution of only the web has been used to estimate the flange edge support stiffness (Barbero et al. 1991; Qiao et al. 2001; Kollár 2003). Nonetheless, the elastic rotational restraint provided by the flange-web junction is known to have an impact on the FLB behavior of pGFRP sections. Some studies have demonstrated that flange-web junctions having low rotational stiffness and strength could lead to premature failure of the entire pGFRP structural profile (Bank and Yin 1999; Turvey and Zhang 2006a; Feo et al. 2013). In order to assess the elastic rotational behavior of the flange-web junction of the pGFRP box-sections used in this work, digital images were used and an experimental test was conducted. Results were compared to the theoretical values obtained using Eq. 4. Finally, the resulting stiffness, considering both the flange-web junction and web, was calculated.

A simple method of assessing fiber architecture of specimens was used in this study. Instead of complex imaging techniques, digital images of thin sections cut from the end of test specimens are obtained. The thin sections are placed on a mobile telephone screen or similar ‘light table’ with a white page showing. The light is easily transmitted through the longitudinal fiber but not the matrix and embedded continuous strand mat (CSM). The resulting images, an example of which is shown in Figure 3, are analyzed to determine both fiber content and architecture – the location of the fiber in the cross section. While not the

focus of this work, this simple method is proposed to allow the immediate, rapid and economic assessment of specimen fiber architecture.

In Figure 3, it can be clearly seen that the fiber-matrix architecture is not as uniform as expected: the fiber rovings are intermittent; in addition, only two layers of rovings were observed, while there should be three. Qualitatively, based on images like Figure 3, it is hypothesized that the rotational restraint of the flange plate provided by the web at this junction is uncertain, likely closer to the pinned condition, and likely highly variable.

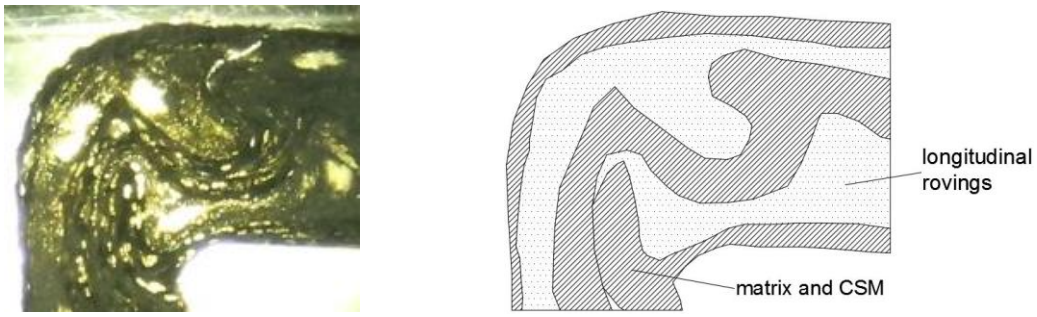

a) Image of fiber and matrix architecture b) Schematic of fiber and matrix architecture

Figure 3 Fiber and matrix architecture at flange-web junction of specimen B1

As if to reinforce this uncertainty and the potential weakness of the flange-web junction, Specimen B1-F1-700 exhibited a failure, shown in Figure 4, in this region. This failure occurred immediately following FLB at an applied moment of 13400 Nm. Although FLB had occurred, this moment capacity is barely half the expected moment capacity of the box section and should therefore be considered to be an undesirable 'premature' failure mode.

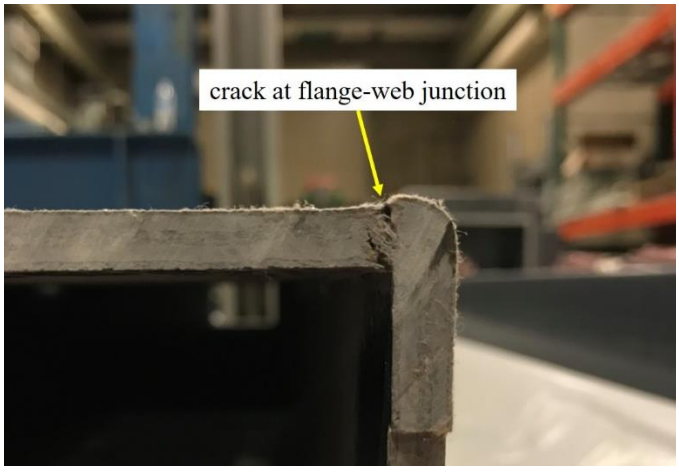

Figure 4 Crack at the flange-web junction occurred in test B1-F1-700

Experimental assessment of the flange-web junction stiffness was conducted using the test method proposed by Turvey and Zhang (2006b), shown in Figure 5. For a box section, this method is used to determine the flexural stiffness of the web-flange junction by clamping a channel-shaped specimen (box section with one flange removed) between two rigidly restrained plates and applying a point load, *P*, at the midspan of the specimen. The flange plate is therefore elastically restrained at its ends by the web-flange junctions. From the recorded vertical displacement at midspan, Δ, the elastic rotational stiffness of the flange-web junction, *k*, can be calculated from Eq. 10[1].

$$k_{exp} = \frac{1}{h}\frac{\frac{E_T h t_f^3}{6L}}{\frac{1}{2\left(1 - 4\frac{E_T h t_f^3}{L^3}\frac{\Delta}{P}\right)} - 1} \tag{10}$$

Where E_T is transverse modulus of elasticity (see Table 2); h, t_f and L are shown in Figure 5; P is the applied load at midspan and Δ is the corresponding displacement at midspan. Four channel-shaped specimens cut from the 102 x 152 x 6.4 mm box sections used in this study were tested. Measured properties are given in Table 1; thus, in Eq. 10, t_w = 6.5 mm, $L = d - 2t_w$ =139.3 mm, and a 25 mm length of box was used; thus h = 25 mm.

Test results are shown in Table 5. It can be seen that the thicker flange F1 has a greater rotational stiffness, $k_{exp,}$ at the flange-web junction than flange F2. The experimentally determined value of k_{exp} is less than one-third of the theoretically calculated value (Eq. 4) indicating that the rotational restraint provided by the web-flange junctions in the box sections test is less than the stiffness of web, which has been commonly used to evaluate the stiffness of flange edge support. The variability of the junction region (Figure 3) and other material and geometric imperfections also contribute to this difference.

The experimentally determined rotational stiffness of flange-web junction, k_{exp}, was further combined with the k factor accounting for the web stiffness (Eq. 4) to calculate the effective stiffness of flange edge support, k_{eff}, as presented in Eq. 11. Results are presented in Table 5.

$$k_{eff} = \frac{k_{exp} + k}{k_{exp} k} \tag{11}$$

In addition, k_{eff} was substituted into Eq. 7 and the resulting critical FLB moments were obtained, as shown on the right side of Table 4. It is evident in using k_{eff} that the FLB predictions for the box-sections shows

[1] It is noted that Eq. 7 in Turvey and Zhang (2006b) in terms of the load-strain relationship is correct, however Eq. 8, which defines the stiffness in terms of load-displacement (Δ/*P*) contains a typographic error which is corrected in the present work in Eq. 10.

improved accuracy when compared with the predictions calculated using the analytically determined k factor. Additionally, using k_{exp} leads to parameters α = 2.36 and β = 2.01 for flange F1 and α = 2.44 and β = 2.01 for flange F2 (Table 5). This, again, demonstrates that the actual rotational stiffness of the flange-web junction of the box-sections used in this work is closer to being a simply-supported boundary condition, namely the lower bound solution ($\alpha = \beta = 2$).

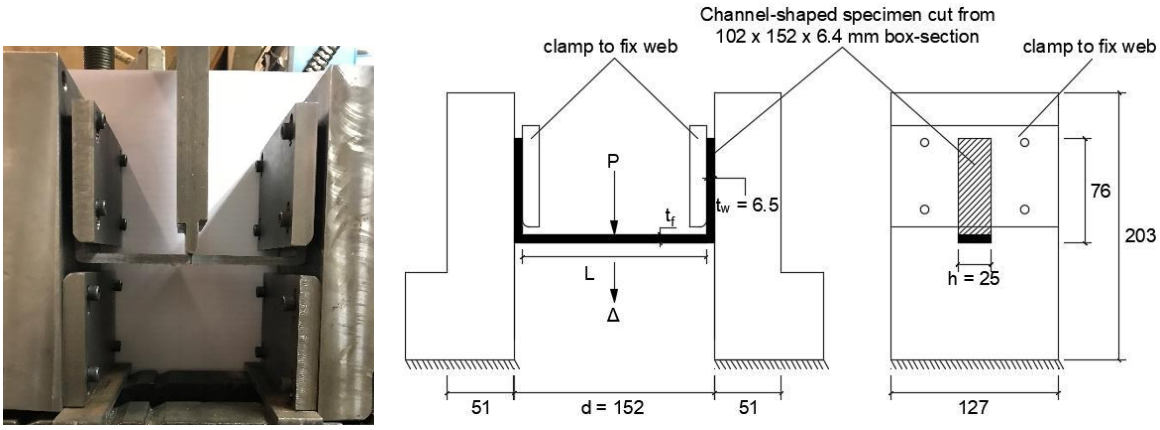

a) Test set-up b) Schematic view (all dimensions in mm)

Figure 5 Test set-up for rotational stiffness of flange-web junction

Table 5 Channel-shaped specimen geometries and flange-web junction stiffness (COV in brackets)

Specimen	L (mm)	h (mm)	t_f (mm)	Δ/P (mm/N)	k_{exp} (Eq. 10) (N/rad)	α (Eq. 8)	β (Eq. 9)	k (Eq. 4) (N/rad)	k_{eff} (Eq. 11) (N/rad)
F1	139.23	24.55	7.02	0.0170 (0.37)	3213 (0.15)	2.45	2.01	10430	2456
F2	139.26	26.83	6.01	0.0404 (0.27)	2468 (0.06)	2.51	2.01	10768	2008

Conclusions

In this work, an experimental program was conducted to investigate the flange local buckling (FLB) behavior of pGFRP box-sections. Experimentally determined critical FLB moments were reported. The commonly accepted design equation based on plate theory (Kollár 2003) was validated although importance of accurate assessment of the rotational stiffness of the web-flange junctions was identified. It is concluded that the lower bound solution, using $\alpha = \beta = 2$, promulgated by EUR 27666 (2016) results in uniformly conservative predictions of the critical FLB moments. The so-called 'exact' solution given by Kollár (2003) and adopted by ASCE (2010), over-predicts the stiffness of the flange edge supprt resulting in unconservative predictions when compared with the experimental results.

The rotational stiffness of flange-web junction of the pGFRP box-section addressed in this work investigated experimentally. It is found that the actual rotational stiffness of flange-web junction is

relatively low, closer to simply-supported boundary condition. It is also proposed that theoretical prediction of this stiffness considering only material and geometric properties neglects the effects of fibre architecture in the web-flange transition which has been shown to be highly variable. This observation supports the use of the lower bound solution, given as Eq. 7 with $\alpha = \beta = 2$ for design of pGFRP box-sections.

Acknowledgement

The authors wish to thank Bedford Reinforced Plastics for providing pGFRP materials used in this work.

References

American Society of Civil Engineers. (ASCE). (2010). *Pre-Standard for Load and Resistance Factor Design (LRFD) of Pultruded Fiber Reinforced Polymer (FRP) Structures*.

Ascione L, Caron J F, Godonou P, van IJselmuijden K, Knippers J, Mottram T, Oppe M, Gantriis Sorensen M, Taby J, Tromp, L. (2016). *Prospect for new guidance in the design of FRP*; EUR 27666.

Ascione, F., Feo, L., Lamberti, M., Minghini, F., & Tullini, N. (2016). A closed-form equation for the local buckling moment of pultruded FRP I-beams in major-axis bending. *Composites Part B: Engineering*, 97, 292-299.

ASTM Standard D695-15 (2015). Standard Test Method for Compressive Properties of Rigid Plastics, ASTM International, West Conshohocken, PA.

ASTM Standard D3039/D3039M-14 (2014). Standard Test Method for Tensile Properties of Polymer Matrix Composite Materials. ASTM International, West Conshohocken, PA.

ASTM Standard D3518/D3518M-13 (2013). Standard Test Method for In-Plane Shear Response of Polymer Matrix Composite Materials by Tensile Test of a ±45° Laminate. ASTM International, West Conshohocken, PA.

ASTM Standard ASTM D7264/D7264M-15 (2015). Standard Test Method for Flexural Properties of Polymer Matrix Composite Materials, ASTM International, West Conshohocken, PA.

Bank, L. C., & Yin, J. (1999). Failure of web-flange junction in postbuckled pultruded I-beams. *Journal of Composites for Construction*, 3(4), 177-184.

Bank, L. C., Gentry, T. R., & Nadipelli, M. (1996). Local buckling of pultruded FRP beams-analysis and design. *Journal of reinforced plastics and composites*, 15(3), 283-294.

Barbero, E. J., Fu, S. H., & Raftoyiannis, I. (1991). Ultimate bending strength of composite beams. *ASCE Journal of Materials in Civil Engineering*, 3(4), 292-306.

Bedford Reinforced Plastics. (2012). *Bedford Reinforced Plastics Design Guide*.

Cardoso, D. C., & Vieira, J. D. (2017). Comprehensive local buckling equations for FRP I-sections in pure bending or compression. *Composite Structures*, 182, 301-310.

Cardoso, D.T.C. (2014) Compressive Strength of Pultruded Glass-Fiber Reinforced Polymer (GFRP) Columns, *PhD Dissertation*, Universidade Federal do Rio de Janeiro, 192 pp.

Cardoso, D., Harries, K.A. and Batista, E. (2014a). Compressive Strength Equation for GFRP Square Tube Columns, *Composites Part B: Engineering* 59, 1-11

Cardoso, D., Harries, K.A. and Batista, E. (2014b) Closed-Form Equations for Local Buckling of Pultruded Thin-Walled Sections, *Thin-walled Structures*, 79, 16-22.

Correia, J. R., Branco, F. A., Silva, N. M. F., Camotim, D., & Silvestre, N. (2011). First-order, buckling and post-buckling behaviour of GFRP pultruded beams. Part 1: Experimental study. *Computers & Structures*, 89(21), 2052-2064.

Feo, L., Mosallam, A. S., & Penna, R. (2013). Mechanical behavior of web–flange junctions of thin-walled pultruded I-profiles: an experimental and numerical evaluation. *Composites Part B: Engineering*, 48, 18-39.

Hashem, Z. A., Yuan, R. L. (2001) Short vs long column behavior of pultruded glass-fiber reinforced polymer composites, *Construction and Building Materials*, 15, 369-378.

Kollár, L. P. (2003). Local buckling of fiber reinforced plastic composite structural members with open and closed cross sections. *ASCE Journal of Structural Engineering*, 129(11), 1503-1513.

Lekhnitskii, S. G. (1968) *Anisotropic plates*, Gordon and Breach Science Publishers, New York

Liu, T., Harries, K.A. and Guo, Q. (2018) Effects of Fiber Architecture on Flexure Properties of Pultruded GFRP Plates and Sections, In *Proceedings of the 9th International Conference on Fibre-Reinforced Polymer Composites in Construction (CICE 2018)*, Paris, July 2018.

Liu T., (2017). *Stability Behavior of Pultruded Glass-Fiber Reinforced Polymer I-Sections Subject to Flexure*, Doctoral dissertation, University of Pittsburgh.

Liu T., Cardoso D. T., Vieira J. D., and Harries K. A. (2017). Convenient and Inexpensive Test Methods for Pultruded GFRP Composite Materials. *Advanced Composites in Construction*. Sheffield, UK, September 2017.

Pecce, M., & Cosenza, E. (2000). Local buckling curves for the design of FRP profiles. *Thin-walled structures*, 37(3), 207-222.

Qiao, P., Davalos, J. F., & Wang, J. (2001). Local buckling of composite FRP shapes by discrete plate analysis. *ASCE Journal of Structural Engineering*, 127(3), 245-255.

Seangatith, S., Sriboonlue, W. (1999) Axially loaded glass-fiber reinforced plastic composite columns, *Seventh East Asia-Pacific Conference on Structural Engineering & Construction*, Kochi, Japan, 1307-1312.

Turvey, G. J., & Zhang, Y. (2006a). A computational and experimental analysis of the buckling, postbuckling and initial failure of pultruded GRP columns. *Computers & structures*, 84(22), 1527-1537.

Turvey, G. J., & Zhang, Y. (2006b). Characterisation of the rotational stiffness and strength of web-flange junctions of pultruded GRP WF-sections via web bending tests. *Composites Part A: applied science and manufacturing*, 37(2), 152-164.

Vieira, J. D., Liu, T., & Harries, K. A. (2017). Flexural stability of pultruded glass fibre-reinforced polymer I-sections. *Proceedings of the Institution of Civil Engineers-Structures and Buildings*, 1-12. http://dx.doi.org/10.1680/jstbu.16.00238

Zureick, A., Scott, D. (1997) Short-term behavior and design of fiber-reinforced polymeric slender members under axial compression, *ASCE Journal Composites for Construction*, 1(4), 140-149.

Appendix A: Experimental Results

In order to capture the onset of the flange local buckling behavior, three electrical resistance strain gages were used on each specimen. The strain gage layout is shown in Figure 1b. The moment – strain relationship obtained from each test is shown in Figure A. The observed critical FLB moment, M_{cr}, is also presented. Self-weight of the specimen, 0.05 kN/m, was added to calculate the critical FLB moment, M_{cr}.

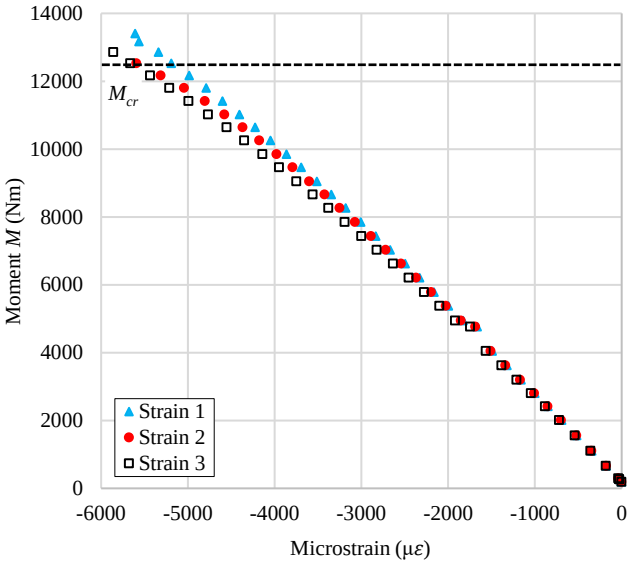

a) B1-F1-700 (M_{cr} = 12558 Nm)

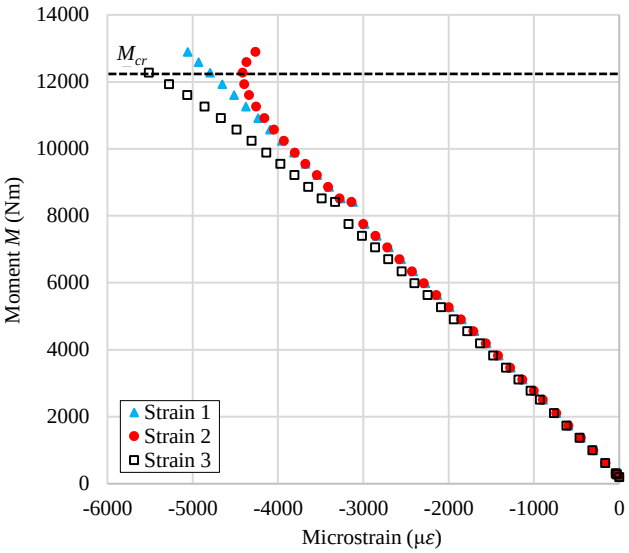

b) B1-F1-800 (M_{cr} = 12310 Nm)

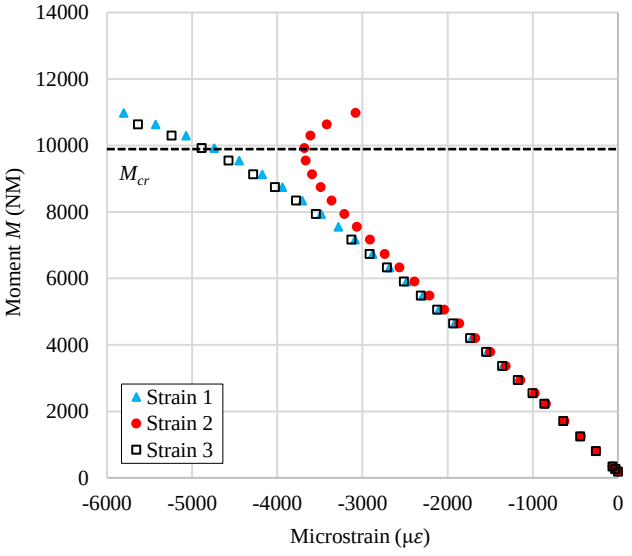

c) B1-F2-700 (M_{cr} = 9954 Nm)

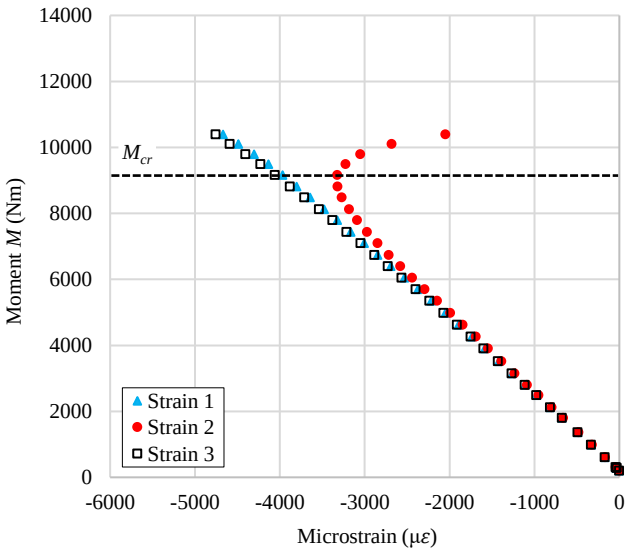

d) B1-F2-800(M_{cr} = 9207 Nm)

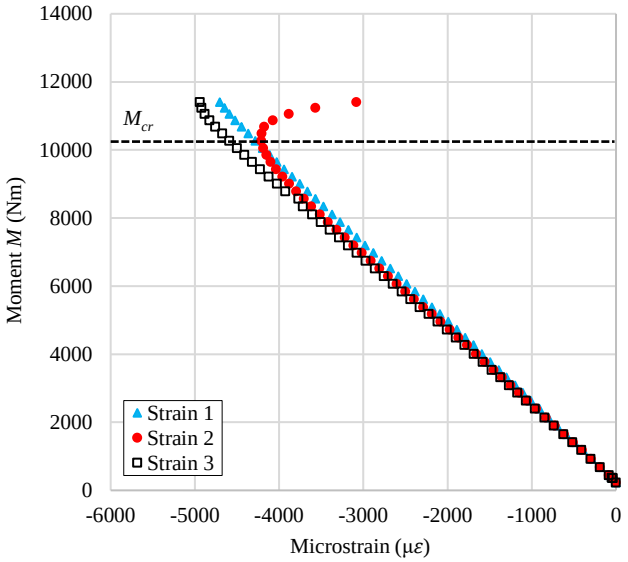

e) B2-F1-900 (M_{cr} = 10315 Nm)

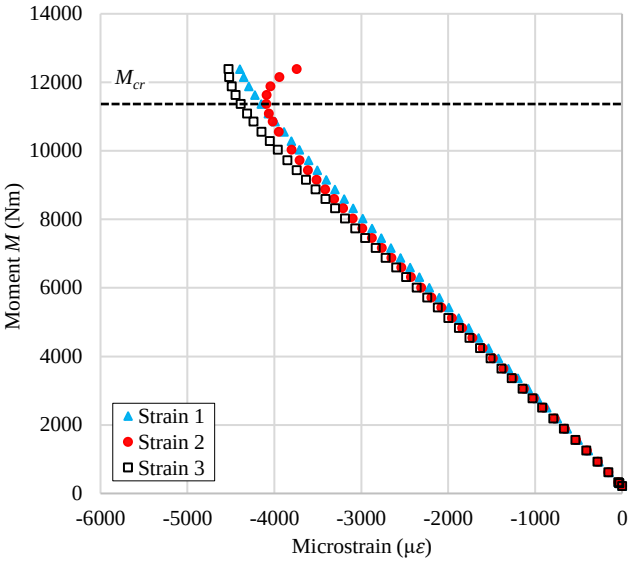

f) B2-F1-1000 (M_{cr} = 11414 Nm)

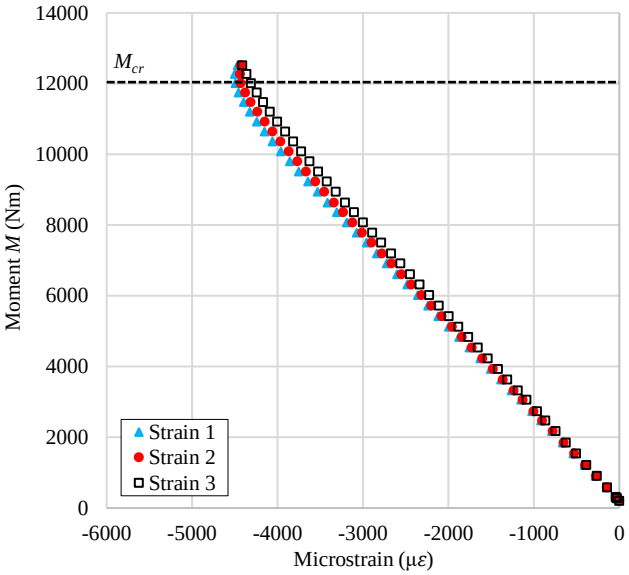

g) B2-F1-1100 (M_{cr} = 12059 Nm)

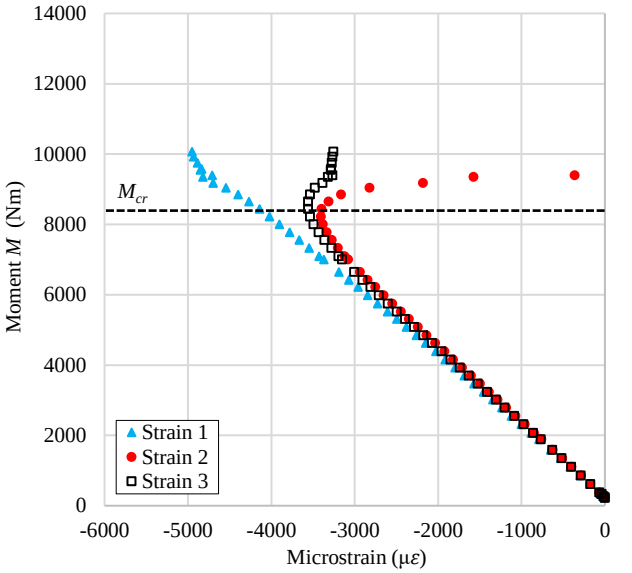

h) B2-F2-900 (M_{cr} = 8267 Nm)

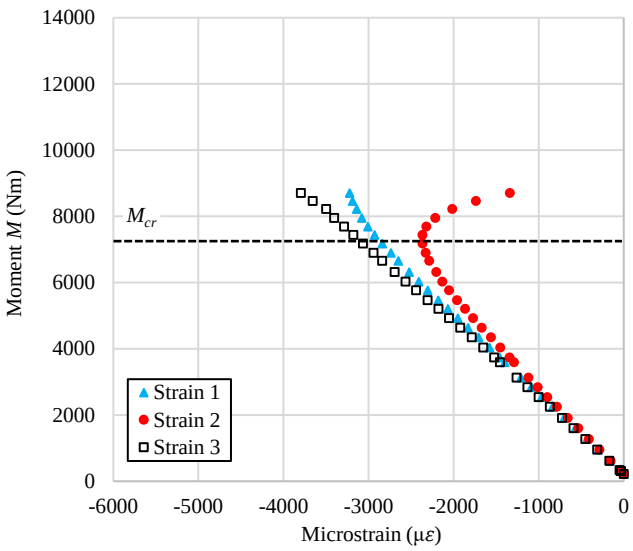

i) B2-F2-1000 (M_{cr} = 7216 Nm)

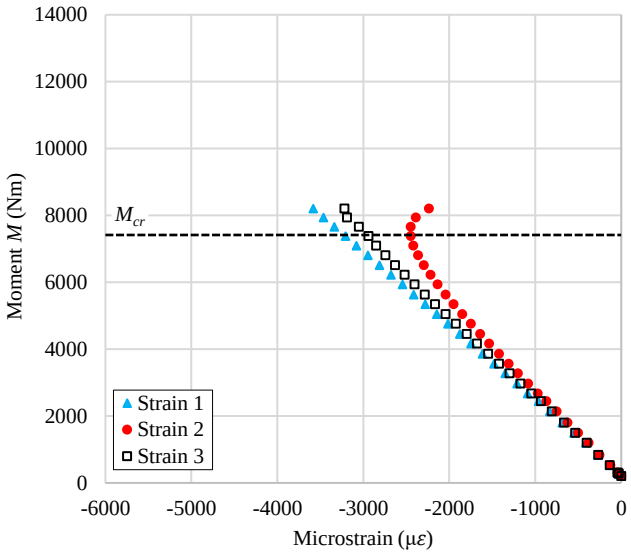

j) B2-F2-1100 (M_{cr} = 7425 Nm)

Figure A Moment – strain relationship of each test